Manipulating topological inner-edge states in hybrid silicene nanoribbons

Yafang Xu[1,2] and Guojun Jin[1,3,*]

[1]*National Laboratory of Solid State Microstructures, Department of Physics, and Collaborative Innovation Center of Advanced Microstructures, Nanjing University, Nanjing 210093, China*

[2]*College of Physics Science and Technology, Yangzhou University, Yangzhou 225002, China*

[3]*Department of Physics Science and Technology, Kunming University, Kunming 650214, China*

(Received 22 November 2016; revised manuscript received 3 February 2017; published 17 April 2017)

Edge states in quantum spin Hall insulators have important applications in low-dissipation devices. However, the breaking of the valley degree of freedom for finite-sized nanoribbons violates the formation of gapless valley edge states. In this work, we investigate the topological and transport properties in a hybrid silicene nanoribbon, two halves of which are in different topological phases modulated by external perpendicular electric fields and antiferromagnetic exchange fields independently. By observing the inner-edge states, different band insulators, especially the quantum spin and valley Hall insulators, can be distinguished. Special inner-edge states, such as single valley or spin-valley channels, cause the valley thermal rectification effect, which can be used to design topological thermal diodes. Furthermore, we calculate the thermoelectric performance of inner-edge states with a dual scattering time model and find an enhancement compared with the original topological edge states at a higher temperature. These spin- and valley-resolved inner-edge states may facilitate more applications in topological valley electronics and thermoelectronics.

DOI: 10.1103/PhysRevB.95.155425

I. INTRODUCTION

As a member of the same group as carbon, just like graphene, silicon was also fabricated successfully into one-atom-thick sheet on some metal substrates [1–3]. It is the so-called silicene, which attracts lots of attention for its band topology and unique transport properties [4–11]. Silicene has more merits than graphene; for example, it has a relatively large spin-orbit coupling [6] and better compatibility with current silicon-based technology. It has been found that under the modulation of different external fields, such as electric [4], magnetic [7], and light [8] fields, silicene undergoes various topological phases. In Ref. [12], Ezawa has summarized a table which lists all the possible topological phases and the corresponding Chern numbers.

In conventional semiconductors, the two degrees of freedom, spin and charge, play prominent roles in fundamental physics and real applications. With the advent of graphene which has two nonequivalent sublattices, another intrinsic degree of freedom, i.e., valley, makes valleytronics a new subject [13]. As more two-dimensional (2D) materials emerge, such as silicene and transition metal dichalcogenides [14], valleytronics has developed rapidly. Valley is a good degree of freedom for a large sheet of material, where the valley Chern number and spin-valley Chern number can be well described.

It can be understood that helical edge states in silicene nanoribbons have potential applications in low-loss devices. However, the valley degree of freedom is destroyed due to size limitation. Hence, it is difficult to characterize the quantum valley Hall insulator and quantum spin-valley Hall insulator by observing the topological edge states. Especially, for the quantum spin-valley Hall insulator $(C_{\uparrow}^{K'}, C_{\downarrow}^{K'}, C_{\uparrow}^{K}, C_{\downarrow}^{K}) = \pm(-1/2, 1/2, 1/2, -1/2,)$, it cannot even be distinguished by the commonly used Hall-bar equipment [15,16], because each valley ($C^{K(K')} = C_{\uparrow}^{K(K')} + C_{\downarrow}^{K(K')}$) and spin ($C_{\uparrow(\downarrow)} = C_{\uparrow(\downarrow)}^{K} + C_{\uparrow(\downarrow)}^{K'}$) Chern number is zero. How to realize the topological valley edge states and manipulate them to achieve good performance in device applications is an important and interesting issue. It has been indicated that by constructing a hybrid silicene nanoribbon with different topological phases, the topological valley edge states can appear on the inner-edge [12].

In this work, we investigate a hybrid silicene nanoribbon, composed of two adjacent topological insulators determined by different electric fields and antiferromagnetic exchange fields. We propose to distinguish the band insulators with nontrivial spin and valley Chern numbers by using a convenient method to observe their inner-edge states. We obtain a spin- and valley-dependent single channel by tuning external fields and utilize it to reach a topological thermal rectification diode. Furthermore, we calculate the thermal power and figure of merit of spin- and valley-dependent topological edge states and show an enhancement in the thermoelectric performance at a higher temperature, compared with the contribution from the original helical topological edge of natural silicene.

The rest of the paper is organized as follows. In Sec. II, we present the model and formalism with emphasizing the Chern numbers to describe corresponding topological phases. In Sec. III, an approach is proposed for characterizing the band insulators with spin- and valley-resolved inner-edge states. A thermal rectification diode based on the topological inner-edge states is designed and described in Sec. IV. In Sec. V, we calculate the thermoelectric performance of inner-edge states and compare the results with the original helical edge states of quantum spin Hall insulators. Finally, the conclusion of this work is given in Sec. VI.

II. MODEL AND FORMALISM

A hybrid silicene nanoribbon is shown in Fig. 1. The upper and bottom half-nanoribbons are modulated by different perpendicular electric fields and antiferromagnetic exchange

*gjin@nju.edu.cn

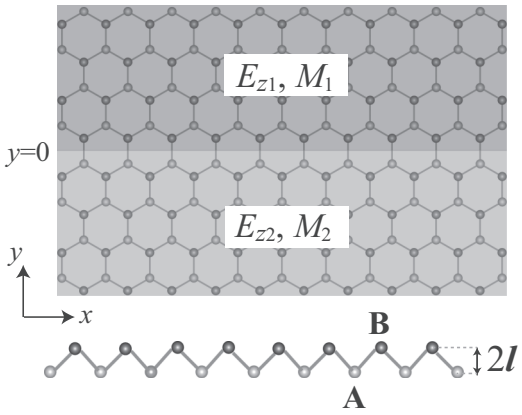

FIG. 1. Schematic of a hybrid silicene nanoribbon. Two different perpendicular electric fields and antiferromagnetic exchange fields are applied in the upper and lower half-nanoribbons. In the side view, the buckled distance of A and B sublattices is $2l = 0.46$ Å.

fields. The exchange field can arise by proximity coupling to a honeycomb-lattice antiferromagnet [17,18], which acts on two sublattices separately. In the tight-binding model, the Hamiltonian of the system is described by [4,8]

$$\mathcal{H} = -t \sum_{\langle i,j\rangle\alpha} c^{\dagger}_{i\alpha} c_{j\alpha} + i \frac{\lambda_{\rm SO}}{3\sqrt{3}} \sum_{\langle\langle i,j\rangle\rangle\alpha\beta} \nu_{ij} c^{\dagger}_{i\alpha} s^{z}_{\alpha\beta} c_{j\beta} + \mathcal{H}_{\rm f}(y), \tag{1}$$

where $c_{i\alpha}$ ($c^{\dagger}_{i\alpha}$) annihilates (creates) an electron with spin α at site i; the sum is taken over all the nearest-neighboring $\langle i,j\rangle$ and next-nearest-neighboring $\langle\langle i,j\rangle\rangle$ sites; $s^{z}_{\alpha\beta}$ is the z component Pauli matrix of spin and α and β are the spin indices; $\lambda_{\rm so} = 3.9$ meV is the spin-orbit coupling strength; when the next-nearest-neighboring hopping is clockwise, $\nu_{ij} = -1$, otherwise, $\nu_{ij} = 1$; the term $\mathcal{H}_{\rm f}(y)$ represents the Hamiltonian of the external field contributions, where the fields are spatially different in the upper and bottom half-nanoribbons along the y direction.

We denote the electric field as E_{z1} (E_{z2}) and antiferromagnetic exchange field M_1 (M_2) in the upper (lower) half-ribbon. The term $\mathcal{H}_{\rm f}(y)$ can be written in a uniform form,

$$\begin{aligned}\mathcal{H}_{\rm f}(y) = &-[\Theta(y) l E_{z1} + \Theta(-y) l E_{z2}] \sum_{i\alpha} \mu_i c^{\dagger}_{i\alpha} c_{i\alpha} \\ &+ [\Theta(y) M_1 + \Theta(-y) M_2] \sum_{i\alpha\beta} \mu_i c^{\dagger}_{i\alpha} s^{z}_{\alpha\beta} c_{i\beta},\end{aligned} \tag{2}$$

where $\mu_i = 1$ (-1) corresponds to the A (B) sublattice, and $\Theta(y)$ is the Heaviside function.

In the low-energy approximation, the Hamiltonian of the hybrid nanoribbon can be written in momentum space as

$$\mathcal{H} = \hbar v_{\rm F}(\eta\sigma_x k_x + \sigma_y k_y) + \eta\sigma_z s_z \lambda_{\rm so} + F_{\rm ext}\sigma_z, \tag{3}$$

where $\eta = \pm 1$ are for K and K' valleys, $s_z = \pm 1$ are the spin indexes, and

$$\begin{aligned}F_{\rm ext} = &-[\Theta(y) l E_{z1} + \Theta(-y) l E_{z2}] \\ &+ [\Theta(y) M_1 + \Theta(-y) M_2] s_z.\end{aligned} \tag{4}$$

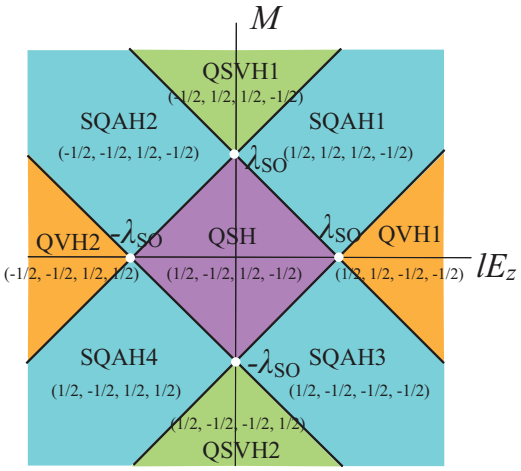

FIG. 2. Phase diagram of a silicene nanoribbon with homogeneous perpendicular electric field and antiferromagnetic exchange field. Each region is labeled by a set of spin- and valley-dependent Chern numbers $(C^{K'}_{\uparrow}, C^{K'}_{\downarrow}, C^{K}_{\uparrow}, C^{K}_{\downarrow})$. The topological phases are spin quantum anomalous Hall (SQAH), quantum spin-valley Hall (QSVH), quantum valley Hall (QVH), and quantum spin Hall (QSH) insulators, respectively.

By diagonalizing Eq. (3), the band structure of the system can be obtained as

$$E_{\eta s_z} = \pm\sqrt{(\hbar v_{\rm F} k)^2 + (\eta s_z \lambda_{\rm so} + F_{\rm ext})^2}. \tag{5}$$

For each half of the nanoribbon, the phase transition is determined by the gap of the band structure. The gap is given as

$$\Delta_{1(2)} = 2(\eta s_z \lambda_{\rm so} - l E_{z1(2)} + s_z M_{1(2)}). \tag{6}$$

Because the Rashba spin-orbit interactions are small and neglected [8], the spin index s_z is a good quantum number, then Chern number can be used to characterize the topological quantum properties. It is explicitly written as

$$C_{1(2)\eta s_z} = \frac{\eta}{2} \,\mathrm{sgn}(\eta s_z \lambda_{\rm so} - l E_{z1(2)} + s_z M_{1(2)}). \tag{7}$$

The charge, spin, valley, and spin-valley Chern numbers are defined as $C = \sum_{\eta,s_z} C_{\eta,s_z}$, $C_{\rm s} = \frac{1}{2}\sum_{\eta}(C_{\eta,+1} - C_{\eta,+1})$, $C_{\rm v} = \sum_{s_z}(C_{+1,s_z} - C_{-1,s_z})$, and $C_{\rm sv} = \frac{1}{2}(C_{+1,+1} - C_{-1,+1} - C_{-1,+1} + C_{-1,-1})$, respectively. In order to understand the results below more clearly, we review the phase diagram of a nanoribbon with perpendicular electric field and antiferromagnetic exchange field [18]. In Fig. 2, each topological phase is indexed by a set of spin- and valley-dependent topological Chern numbers $(C^{K'}_{\uparrow}, C^{K'}_{\downarrow}, C^{K}_{\uparrow}, C^{K}_{\downarrow})$. The energies at the intersections of phase boundaries equal $\pm\lambda_{\rm SO}$.

As has been known, the integrity of valley is violated at the edge of a finite-sized nanoribbon, there does not exist a topological valley edge state. However, for a hybrid nanoribbon, there exists an interface between two different topological insulator phases, and the valley degree of freedom at the interface is maintained. The topological edge states at the interface are called inner-edge states [12,19]. Due to the counteraction of Hall currents from two topological insulators, the Chern number of an inner-edge state is equal to the

TABLE I. Charge, spin, valley, and spin-valley Chern numbers of several band insulators.

	C	C_s	C_v	C_{sv}
QVH1	0	0	2	0
QVH2	0	0	−2	0
QSVH1	0	0	0	1
QSVH2	0	0	0	−1

difference between the topological quantum numbers of two adjacent regions [12]. Specifically, ΔC, ΔC_s, ΔC_v, and ΔC_{sv} are the charge, spin, valley, and spin-valley Chern numbers of an inner state, respectively. For such a hybrid nanoribbon with different external fields, the spin- and valley-dependent Chern numbers of inner-edge states can be described as

$$\Delta C_{\eta s_z} = C_{1\eta s_z} - C_{2\eta s_z}. \quad (8)$$

III. BAND INSULATORS WITH INNER-EDGE STATES

A large perpendicular electric field, as well as an antiferromagnetic exchange field can turn silicene into a band insulator [18]. The former breaks the spatial symmetry, and the latter breaks the time-reversal symmetry. In fact, in the phase diagram of Fig. 2, QVH1, QVH2, QSVH1, and QSVH2 are all band insulators. In these insulators, the charge Chern number and spin Chern number are zero. There are no topological edge states appearing in the band structures. However, the valley or spin-valley Chern number is not zero, which can be seen in Table I.

In general, the most straightforward method to distinguish band insulator from topological insulator is to calculate the band structure of a finite-width nanoribbon and observe if topological edge states exist. Different topological phases can also be differentiated by some transport measurements [11,20]. However, for a QSVH insulator, whose Chern numbers are $(C_\uparrow^{K'}, C_\downarrow^{K'}, C_\uparrow^{K}, C_\downarrow^{K}) = \pm(-1/2, 1/2, 1/2, -1/2)$, both methods are unavailable. In order to characterize the band insulator with nontrivial topological quantum numbers, for simplification, we consider two specific hybrid nanoribbons in this section.

In the first case, the hybrid nanoribbon has two independent electric fields, while the exchange field $M_1 = M_2 = 0$. The spin and valley dependent Chern numbers of inner-edge states can be described as

$$\Delta C_{\eta s_z} = \frac{\eta}{2}\,\mathrm{sgn}(\eta s_z \lambda_{so} - lE_{z1}) - \frac{\eta}{2}\,\mathrm{sgn}(\eta s_z \lambda_{so} - lE_{z2}). \quad (9)$$

The phase boundaries are determined by $lE_{z1} = \pm\lambda_{so}$ and $lE_{z2} = \pm\lambda_{so}$, as shown by the red thick lines in Fig. 3(a). In previous researches, the criterion for topological phase transition is the gap closing and reopening. In the present case, once phase transition happens in one half-nanoribbon, the inner-edge states will change. In order to see the edge states, the band structures at several marked points of phase diagram are shown in Fig. 3(b). It should be noted that, in the numerical calculation, we adopt a zigzag silicene nanoribbon with the width $W = 128$ atoms. Silicene is a quantum spin Hall insulator in the absence of external fields. The band structure can be seen in Fig. 3(b)(1). When both electric fields E_{z1} and E_{z2} are larger than the critical electric field, the system

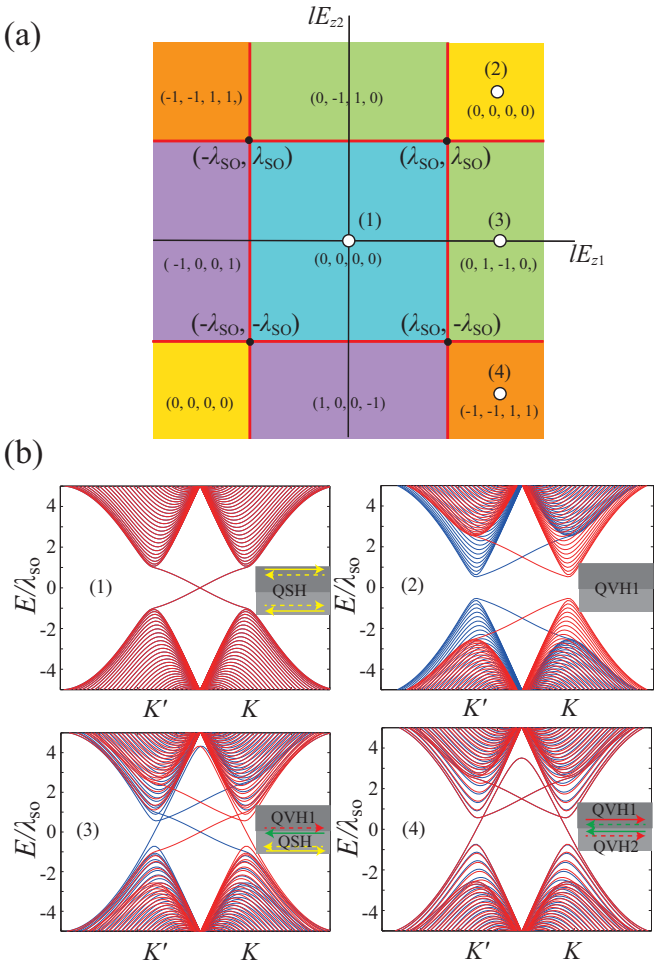

FIG. 3. Phase diagram of a hybrid silicene nanoribbon with independent perpendicular electric fields E_{z1} and E_{z2}, while $M_1 = M_2 = 0$. The indexes in each region are the spin and valley Chern numbers of inner-edge states. (b) The band structure of a hybrid silicene nanoribbon at marked points in the phase diagram (a).

is in the band insulator phase, shown by the band structure in Fig. 3(b)(2), but it has nontrivial valley Chern numbers, which are $(C_\uparrow^{K'}, C_\downarrow^{K'}, C_\uparrow^{K}, C_\downarrow^{K}) = (-1/2, -1/2, 1/2, 1/2)$. If the hybrid nanoribbon is constructed by QSH and QVH1, for example the white dot (3) in Fig. 3(a), the band structure can be seen in Fig. 3(b)(3). The inner-edge states appear. At the interface, the electrons in K' valley with spin down move to the right and electrons in K valley with spin up move to the left. The channels can be seen in the inset, where red (green) arrows denote the K' (K) valley inner-edge channels, yellow arrows represent the outer-edge channels, and solid (dashed) lines denote the spin up (down) channels. In this case, the domain wall can be used as a spin-valley filter. We then change the direction of the electric field in one half-nanoribbon; the band structure of the QVH1/QVH2 nanoribbon is shown in Fig. 3(b)(4). The outer-edge states disappear and only inner-edge states exist, just as shown in the inset of Fig. 3(b)(4). The inner-edge states are valley resolved but spin degenerate. By observing the edge states, the quantum valley Hall insulator can be detected.

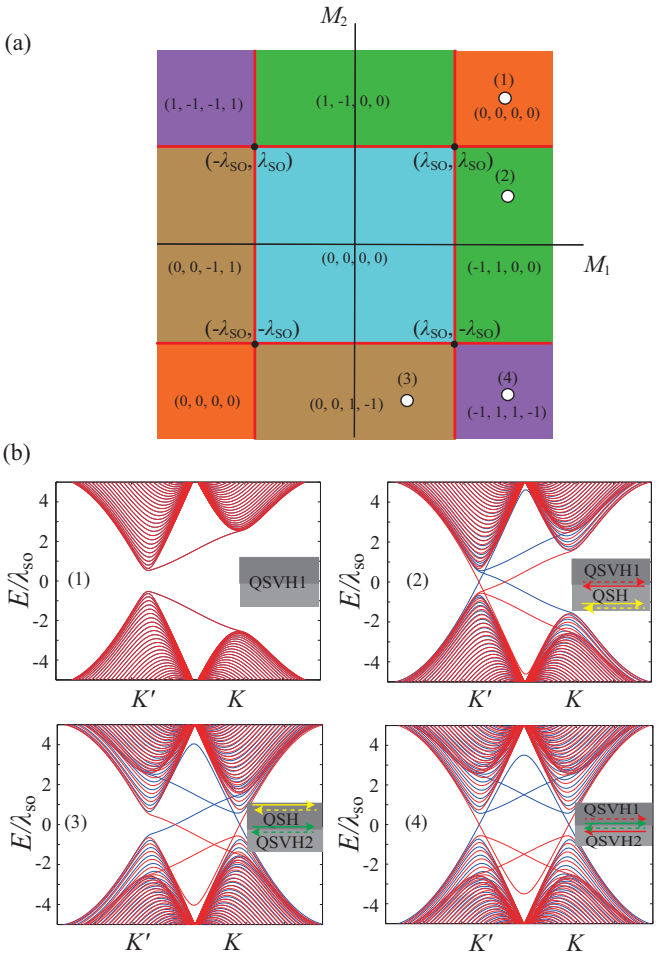

FIG. 4. Phase diagram of a hybrid silicene nanoribbon with independent antiferromagnetic exchange fields M_1 and M_2, while $E_{z1} = E_{z2} = 0$. The indexes in each region are the spin and valley Chern numbers of inner-edge states. (b) The band structures of the hybrid silicene nanoribbon at the marked points in the phase diagram (a).

In the second case, the hybrid nanoribbon is applied by two independent antiferromagnetic exchange fields, while electric fields $E_{z1} = E_{z2} = 0$, and the spin- and valley-dependent Chern number of an inner-edge state is given as

$$\Delta C_{\eta s_z} = \frac{\eta}{2}\mathrm{sgn}(\eta s_z \lambda_{so} + s_z M_1) - \frac{\eta}{2}\mathrm{sgn}(\eta s_z \lambda_{so} + s_z M_2), \tag{10}$$

The phase boundaries are determined by $M_1 = \pm\lambda_{so}$ and $M_2 = \pm\lambda_{so}$, which are shown by the red thick lines in Fig. 4(a). When both exchange fields are larger than λ_{so}, i.e., $|M_1|, |M_2| > \lambda_{so}$, the silicene is also a band insulator, but its topological numbers are $(C_\uparrow^{K'}, C_\downarrow^{K'}, C_\uparrow^{K}, C_\downarrow^{K}) = (-1/2, 1/2, 1/2, -1/2)$. It can also be called a quantum spin-valley Hall insulator. The band structure with the tight-binding calculations is shown in Fig. 4(b)(1), and no edge states appear. If we try to utilize the commonly used Hall-Bar equipment to distinguish the quantum spin-valley Hall insulator, because each valley Chern number $C^K = C^{K'} = 0$ and spin Chern number $C_\uparrow = C_\downarrow = 0$, there is no signal to be detected. When the exchange field in one half-nanoribbon is less than the spin-orbit coupling, i.e., the hybrid nanoribbon is constructed by QSVH1 and QSH insulators, the band structure is as shown in Fig. 4(b)(2). Only K valley edge states appears on the inner edge, and the edge states are helical. Certainly, the selection of valley can be achieved by modulating the antiferromagnetic order in different regions, as shown in Fig. 4(b)(3). When both M_1 and M_2 are larger than λ_{so} but with different signs, the upper and lower half-nanoribbons are band insulators, but edge states appear and can be seen in Fig. 4(b)(4). The inner-edge states are spin and valley resolved.

TABLE II. Chern numbers of two hybrid nanoribbons.

QVH1	QVH2	Inner edge state
$(\frac{1}{2},\frac{1}{2},-\frac{1}{2},-\frac{1}{2})$	$(-\frac{1}{2},-\frac{1}{2},\frac{1}{2},\frac{1}{2})$	$(1,1,-1,-1)$
QSVH1	QSVH2	Inner edge state
$(-\frac{1}{2},\frac{1}{2},\frac{1}{2},-\frac{1}{2})$	$(\frac{1}{2},-\frac{1}{2},-\frac{1}{2},\frac{1}{2})$	$(-1,1,1,-1)$

The topological numbers of inner-edge states constructed with two band insulators are shown in Table II. These Chern numbers of the inner-edge states just correspond to the four edge states in Figs. 3(b)(4) and 4(b)(4), and the valley edge state can be demonstrated. Next, we give an analysis to the inner-edge states. Taking into account of the interface at $y = 0$, the wave vector k_x is uniform. In the gap, the energy $|E| < |\Delta_1|$ and $|E| < |\Delta_2|$, the wave function in the upper half-nanoribbon ($y > 0$) can be written as

$$\Psi(y > 0) = c_1 \begin{pmatrix} \frac{\hbar v_F(\eta k_x + i k_{y1})}{E + \Delta_1/2} \\ 1 \end{pmatrix} e^{i k_x x + i k_{y1} y}, \tag{11}$$

and in the lower half-nanoribbon ($y < 0$),

$$\Psi(y < 0) = c_2 \begin{pmatrix} \frac{\hbar v_F(\eta k_x - i k_{y2})}{E + \Delta_2/2} \\ 1 \end{pmatrix} e^{i k_x x - i k_{y2} y}. \tag{12}$$

Obviously, the wave vector $k_{y1(2)}$ is imaginary, as expressed from the dispersion in Eq. (5), $k_{y1(2)} = i\sqrt{(\Delta_{1(2)}/2)^2 + \hbar^2 v_F^2 k_x^2 - E^2}$. According to the continuity condition, the dispersion of the edge state can be obtained. However, it is an implicit function, the solution of which could be obtained by numerical calculations. In the simplified case, taking $M_1 = M_2 = 0$, and $\eta s_z \lambda_{so} - l E_{z1} = l E_{z2} - \eta s_z \lambda_{so}$, the edge states can be determined as $E = \eta \hbar v_F k_x$. They just correspond to the edge states in Fig. 3(b)(4). In the other case, considering $E_{z1} = E_{z2} = 0$ and $\eta\lambda_{so} + M_1 = -M_2 - \eta\lambda_{so}$, the edge states are determined by $E = \eta s_z \hbar v_F k_x$, which can be seen in Fig. 4(d)(4).

IV. TOPOLOGICAL THERMAL RECTIFICATION DIODE

By modulating the external parameters independently in the upper and lower half-nanoribbons, we can manipulate the spin and valley topological edge states. Further, we consider a more general situation where electric and antiferromagnetic fields coexist in the hybrid nanoribbon. It is found that if we construct the hybrid nanoribbon by selecting two topological phases which are adjacent in the phase diagram in Fig. 2, the inner-edge states are spin-valley resolved and the channels are unidirectional. There are 12 kinds of construction methods in total to achieve the single spin-valley channel, but certain

TABLE III. Chern numbers of four hybrid nanoribbons with single spin-valley channel.

QSVH(1-2)	SQAH(1-4)	Inner edge states
$(-\frac{1}{2},\frac{1}{2},\frac{1}{2},-\frac{1}{2})$	$(\frac{1}{2},\frac{1}{2},\frac{1}{2},-\frac{1}{2})$	$(-1,0,0,0)$
	$(-\frac{1}{2},-\frac{1}{2},\frac{1}{2},-\frac{1}{2})$	$(0,1,0,0)$
$(\frac{1}{2},-\frac{1}{2},-\frac{1}{2},\frac{1}{2})$	$(\frac{1}{2},-\frac{1}{2},-\frac{1}{2},-\frac{1}{2})$	$(0,0,0,1)$
	$(\frac{1}{2},-\frac{1}{2},\frac{1}{2},\frac{1}{2})$	$(0,0,-1,0)$

results are degenerate. Four hybrid nanoribbons are listed in Table III, in which the first column corresponds to QSVH1 and QSVH2 and the second column corresponds to SQAH1–SQAH4, successively. If we construct a hybrid nanoribbon with separated topological phases in the phase diagram of Fig. 2, we can obtain a unidirectional valley channel, and there are only two construction methods, which is shown in Table IV. In order to see the inner-edge states clearly, we plot the band structures in Figs. 5(a) and 5(b). In Fig. 5(a), the inner-edge states appear in the K' valley and they are spin resolved; the other edge states connecting two valleys in the band structures are the outer edge states. In Fig. 5(b), the inner-edge state are spin degenerate.

When the incident energy is in the gap, the conductivity is quantized. For a single channel, the quantized conductivity equals e^2/h. We attach the hot and cold electrodes at the two sides of inner-edge states, as shown in Fig. 6(a). For the band structure in Fig. 5(a), the measured thermal conductivity equals $\kappa_e = \pi^2 k_B^2 T/3h$, which obeys the Wiedemann-Franz law [21]. The phonon thermal conductivity is small and neglected. Due to the channel being unidirectional, if we change the direction of the temperature bias, the thermal currents are cut off, and the thermal conductivity is zero. The temperature difference is defined as $\Delta T = T_h - T_c$, and the thermal conductivities are shown in Fig. 6(b). For the inner-edge state in Fig. 5(b), due to spin degeneracy, there are two-channel contributions. The thermal conductivity is double, as can be seen in Fig. 6(b). By the way, if we attach two electrodes with electric bias at the interface of the hybrid nanoribbon, the conductivity is also unidirectional.

V. THERMOELECTRIC PERFORMANCE OF INNER-EDGE STATES

Now, we calculate the thermoelectric performance of inner-edge channels. The Seebeck coefficient is defined as the ratio of voltage difference to the temperature gradient and is written as $S = \nabla\mu/\nabla T$. In the linear response approximation, the electrical current $\boldsymbol{j}$ and thermal current $\boldsymbol{j}_Q$ can be expressed

TABLE IV. Chern numbers of two hybrid nanoribbons with unidirectional valley channel.

SQAH1	SQAH2	Inner edge state
$(\frac{1}{2},\frac{1}{2},\frac{1}{2},-\frac{1}{2})$	$(-\frac{1}{2},-\frac{1}{2},\frac{1}{2},-\frac{1}{2})$	$(1,1,0,0)$
SQAH4	SQAH3	Inner edge state
$(\frac{1}{2},-\frac{1}{2},\frac{1}{2},\frac{1}{2})$	$(\frac{1}{2},-\frac{1}{2},-\frac{1}{2},-\frac{1}{2})$	$(0,0,1,1)$

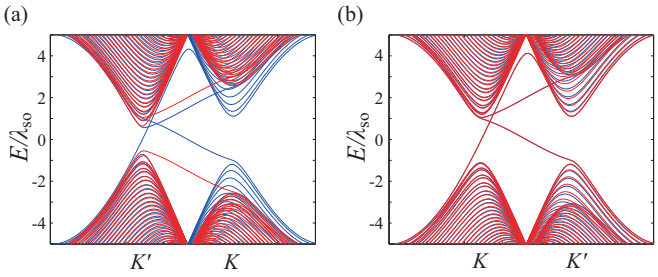

FIG. 5. Band structures of hybrid nanoribbons with (a) QSVH1 ($lE_{z1} = 0, M_1 = 1.5\lambda_{so}$) and SQAH2 ($lE_{z2} = -\lambda_{so}, M_2 = \lambda_{so}$), (b) SQAH1 ($lE_{z1} = \lambda_{so}, M_1 = \lambda_{so}$) and SQAH2 ($lE_{z2} = -\lambda_{so}, M_2 = \lambda_{so}$).

as

$$\begin{pmatrix} \boldsymbol{j}/(-e) \\ \boldsymbol{j}_Q \end{pmatrix} = \begin{pmatrix} L_0 & L_1 \\ L_1 & L_2 \end{pmatrix} \begin{pmatrix} -\nabla\mu \\ -\nabla T/T \end{pmatrix}. \tag{13}$$

With the Onsager coefficients L_α ($\alpha = 0,1,2$), the thermal power, i.e., the Seebeck coefficient, can be given as

$$S = -\frac{1}{eT}\frac{L_1}{L_0}. \tag{14}$$

To explore the effect of topological edge states on the thermoelectrical transport, we use the Landauer transport formula. The integral L_α is written as

$$L_\alpha = \int dE\, T(E)(E-\mu)^\alpha \left(-\frac{\partial f}{\partial E}\right), \tag{15}$$

in which $T(E)$ is the electron transmission function and f the Fermi distribution function. By integral transformation, L_α can be rewritten as

$$L_\alpha = (k_B T)^\alpha \int T(x) x^\alpha \frac{e^x}{(e^x+1)^2} dx, \tag{16}$$

with $x = (E-\mu)/(k_B T)$. The figure of merit can be written as

$$ZT = \frac{L_1^2}{L_0 L_2 - L_1^2 + \kappa_p T L_0}, \tag{17}$$

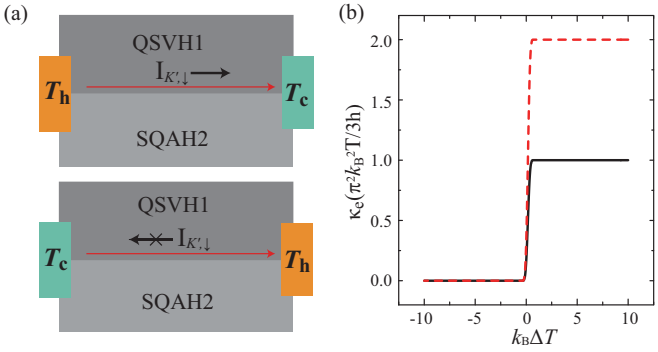

FIG. 6. (a) Schematics of thermal rectification diodes. T_h and T_c denote the hot and cold electrodes, respectively. (b) Quantum thermal conductivity of inner-edge states. The parameters of black solid and red dashed lines correspond to those in Figs. 4(a) and 4(b), respectively.

where κ_p is the phonon thermal conductivity. Due to the edge states being often imperfect but topologically protected, the thermal conductivity from electrons is robust, while the thermal conductivity from phonons is suppressed significantly [22,23]. In a suitable case, the phonon thermal conductivity κ_p at room temperature can be reduced to 0.01 $\mathrm{W\,m^{-1}K^{-1}}$ [23,24], which is smaller by about one order of magnitude than the electron thermal conductivity κ_e. In the calculation, for simplification, we assume that the defects or disorders are strong enough, and only consider the contribution of electrons to the thermal conductivity. In fact, the real figure of merit could be renormalized by the factor $\kappa_e/(\kappa_e+\kappa_p)$, and is lowered slightly, but no fundamental change occurs.

The total transmission function is given as $T(E) = M(E)T_1(E)$ with $M(E)$ being the density of modes, and $T_1(E)$ the transmission probability of each mode [25]. For the topological edge states, $M(E) = N$ counts the forward propagation channels. For a conductor of length L, neglecting the quantum interference effect, the transmission coefficient is obtained as $T_1(E) = \lambda(E)/(\lambda(E)+L)$, where $\lambda(E)$ is the mean free path for backscattering [24]. In the ballistic limit, $T_1(E)$ equals 1, and in the diffusive limit, $T_1(E) = \lambda(E)/L$. We adopt the dual scattering time model to calculate the thermoelectric performance [24]. Within and outside the gap, there exist two different scattering times τ_1 and τ_2, corresponding to the two different mean free paths λ_1 and λ_2. The scattering time ratio is defined as $\tau_r = \tau_1/\tau_2$. We choose the bottom of conduction band as the energy reference point. For the edge state, the integral is given as

$$L_\alpha = (k_B T)^\alpha \left(\int_{-\infty}^{-(|\Delta|+\mu)/k_B T} \frac{\lambda_2(x)}{\lambda_2(x)+L} + \int_{-(|\Delta|+\mu)/k_B T}^{-\mu/k_B T} \frac{\lambda_1(x)}{\lambda_1(x)+L} + \int_{-\mu/k_B T}^{\infty} \frac{\lambda_2(x)}{\lambda_2(x)+L} \right) \times M(x) x^\alpha \frac{e^x}{(e^x+1)^2} dx \quad (18)$$

As a function of temperature, the Seebeck coefficient S and figure of merit ZT are calculated numerically, and the results are shown in Figs. 7(a) and 7(b). It can be seen that S and ZT are reduced at high temperatures. In order to see the the effect of scattering time on the thermoelectric coefficients, we choose three different τ_r as the modulation parameter. The larger τ_r is, the better the thermoelectric performance will be. In experiment, the scattering time can be tuned by introducing defects. Moreover, we plot S and ZT versus chemical potential μ at a relatively low temperature $T = 60$ K in Figs. 7(c) and 7(d). We can give a discussion about the shape of the ZT in Fig. 7(d). The states of energy within about $5k_BT$ around $\mu = 0$ make a dominating contribution to the figure of merit, which approaches zero for large μ. From Eq. (17), according to the Onsager coefficient L_1, the ZT is mainly determined by the factor of $[(E-\mu)\partial f/\partial E]^2$, therefore, the ZT has peaks symmetrically at the two sides of $\mu = -\Delta/2$.

In general, group velocity of electrons is described by $\frac{1}{\hbar}\frac{\partial E}{\partial k}$. For the inner-edge states such as those in Figs. 3(b)(4) and 4(b)(4), $\Delta > 2\lambda_{so}$, they appear on one certain valley. Their velocity approximates the constant $v_F = \sqrt{3}at/2 \approx 5.5\times10^5$ m/s, with $a = 3.86$ Å being the lattice constant, and $t = 1.6$ eV the nearest-neighbor hopping energy. For the conventional helical edge states such as that in Fig. 3(b)(1), they connect two valleys which locate at $K'(K) = -(+)4\pi/3a\hat{\boldsymbol{x}}$ [6]. The velocity nearly equals the gap divided by the distance of two valleys, i.e., $3a\Delta/8\pi$. In this case, in order to ensure the quantum spin Hall phase, the gap is smaller than $2\lambda_{so}$. Hence, the velocity of the inner-edge states is roughly four orders of magnitude higher than that of conventional edge states. Due to $\lambda = v\tau$, for simplification, we set $L/\lambda_1 = 1$ for inner-edge states and $L/\lambda_1 = 10^4$ for the conventional edge states in the calculation.

To make clear the relation between the ZT and gap, and compare the thermoelectric performance of inner and conventional edge states, we present the numerical results

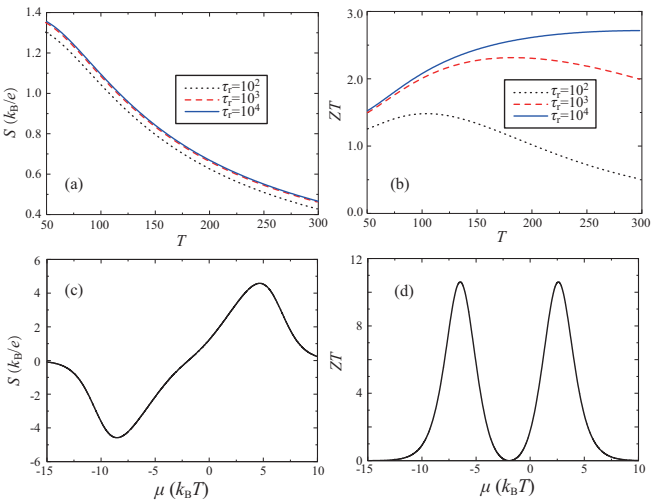

FIG. 7. Temperature dependence of (a) the Seebeck coefficient and (b) the figure of merit ZT of inner-edge states with different time ratios τ_r. The other parameters are $\mu = 0$, $L/\lambda_1 = 1$, and $\Delta = 25$ meV. (c) The Seebeck coefficients and (d) the figure of merit ZT of inner-edge sates as a function of chemical potential. The other parameters are $T = 60$ K, $\tau_r = 10^3$, and $\Delta = 20$ meV.

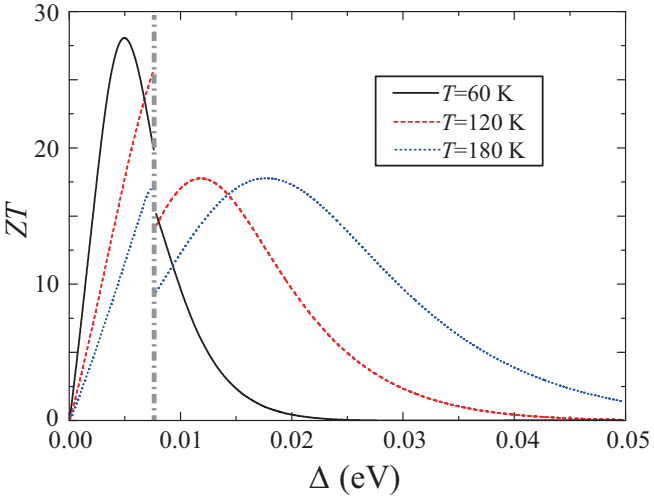

FIG. 8. The ZT of edge states as a function of the gap. The other parameters are $\tau_r = 10^3$ and $\mu = -3/2k_BT$.

plotted in Fig. 8. The phase transition at $\Delta = 2\lambda_{so}$ results in a break of the ZT in Fig. 8, but the variation tendency of the ZT with gap maintains. When the gap is zero, there is no edge state, and the figure of merit is zero naturally. As the gap is large enough, in view of the Mott relation and the reason explained in Ref. [26], ZT is inversely proportional to the gap, and tends to zero also. Hence, ZT does not vary uniformly, but first increases and then decreases with gap. It is obvious that at low temperatures the maximum of ZT locates in the region of $\Delta < 2\lambda_{so}$, but the small gap, as well as the topological edge states, are easily affected by thermal fluctuations. With the temperature increasing, the maximum moves to the region of $\Delta > 2\lambda_{so}$, and the gap correspondingly can be larger. For possible practical applications at higher temperatures, the inner-edge states have advantages in thermoelectrical performance.

VI. CONCLUSION

In summary, we have investigated the spin- and valley-dependent inner-edge states in a hybrid silicene nanoribbon, two halves of which are in different topological phases, and each half is modulated by an independent perpendicular electric field and antiferromagnetic exchange field. It has been proposed that by observing the inner-edge states, different band insulators with nontrivial topological valley Chern number, especially the quantum spin and valley Hall insulators, can be distinguished. By manipulating the external parameters, several special edge states, such as single channel with valley or spin-valley, can be achieved. They cause the thermal rectification effect which can be used to design topological valley diodes. Also, we have calculated the thermoelectric performance of the inner-edge states and found an enhancement compared with that of the conventional edge states at higher temperatures. Based on these results, more possible applications can be expected in topological valley electronics and thermoelectronics.

ACKNOWLEDGMENTS

This work was supported by the State Key Program for Basic Research of China (Grant No. 2015CB921202) and the National Natural Science Foundation of China (Grants No. 11074108 and No. 11504179).

[1] P. Vogt, P. De Padova, C. Quaresima, J. Avila, E. Frantzeskakis, M. C. Asensio, A. Resta, B. Ealet, and G. Le Lay, Phys. Rev. Lett. **108**, 155501 (2012).
[2] A. Fleurence, R. Friedlein, T. Ozaki, H. Kawai, Y. Wang, and Y. Yamada-Takamura, Phys. Rev. Lett. **108**, 245501 (2012).
[3] L. Chen, C.-C. Liu, B. Feng, X. He, P. Cheng, Z. Ding, S. Meng, Y. Yao, and K. Wu, Phys. Rev. Lett. **109**, 056804 (2012).
[4] C.-C. Liu, W. Feng, and Y. Yao, Phys. Rev. Lett. **107**, 076802 (2011).
[5] C.-C. Liu, H. Jiang, and Y. Yao, Phys. Rev. B **84**, 195430 (2011).
[6] N. D. Drummond, V. Zólyomi, and V. I. Fal'ko, Phys. Rev. B **85**, 075423 (2012).
[7] M. Ezawa, Phys. Rev. Lett. **109**, 055502 (2012).
[8] M. Ezawa, Phys. Rev. Lett. **110**, 026603 (2013).
[9] T. Yokoyama, Phys. Rev. B **87**, 241409(R) (2013).
[10] Z. P. Niu and S. Dong, Appl. Phys. Lett. **104**, 202401 (2014).
[11] Y. Xu, X. Zhou, and G. Jin, Appl. Phys. Lett. **108**, 203104 (2016).
[12] M. Ezawa, J. Phys. Soc. Jpn. **84**, 121003 (2015).
[13] D. Xiao, M.-C. Chang, and Q. Niu, Rev. Mod. Phys. **82**, 1959 (2010).
[14] D. Xiao, G.-B. Liu, W. Feng, X. Xu, and W. Yao, Phys. Rev. Lett. **108**, 196802 (2012).
[15] K. Ando and E. Saitoh, Nat. Commun. **3**, 629 (2012).
[16] M. Yamamoto, Y. Shimazaki, I. V. Borzenets, and S. Tarucha, J. Phys. Soc. Jpn. **84**, 121006 (2015).
[17] X. Li, T. Cao, Q. Niu, J. Shi, and J. Feng, Proc. Natl. Acad. Sci. USA **110**, 3738 (2013).
[18] M. Ezawa, Phys. Rev. B **87**, 155415 (2013).
[19] S. Rachel and M. Ezawa, Phys. Rev. B **89**, 195303 (2014).
[20] X. Zhou, Y. Xu, and G. Jin, Phys. Rev. B **92**, 235436 (2015).
[21] H. J. Goldsmid, *Introduction to Thermoelectricity* (Springer, New York, 2010).
[22] R. Takahashi and S. Murakami, Phys. Rev. B **81**, 161302(R) (2010).
[23] S. Murakami, R. Takahashi, O. A. Tretiakov, Ar. Abanov, and J. Sinova, J. Phys. Conf. Ser. **334**, 012013 (2011).
[24] Y. Xu, Z. Gan, and S.-C. Zhang, Phys. Rev. Lett. **112**, 226801 (2014).
[25] R. Kim, S. Datta, and M. S. Lundstrom, J. Appl. Phys. **105**, 034506 (2009).
[26] O. Shevtsov, P. Carmier, C. Groth, X. Waintal, and D. Carpentier, Phys. Rev. B **85**, 245441 (2012).